Supplementary Information

Anisotropic Flow Control and Gate Modulation of Hybrid Phonon-Polaritons

Francisco C. B. Maia,*[,1] Brian T. O'Callahan,[2] Alisson R. Cadore,[3] Ingrid D. Barcelos,[1,3] Leonardo C. Campos,[3] Kenji Watanabe,[4] Takashi Taniguchi,[4] Christoph Deneke,[5,6] Alexey Belyanin[7], Markus B. Raschke,[2] Raul O. Freitas*[,1]

[1]Brazilian Synchrotron Light Laboratory (LNLS), Brazilian Center for Research in Energy and Materials (CNPEM), Zip Code 13083-970, Campinas, Sao Paulo, Brazil.

[2]Department of Physics, Department of Chemistry, and Joint Institute for Lab Astrophysics (JILA), University of Colorado, Boulder, Colorado 80309, United States.

[3]Department of Physics, Federal University of Minas Gerais, 30123-970 – Belo Horizonte, Minas Gerais, Brazil.

[4]Advanced Materials Laboratory, National Institute for Materials Science, 305-0044 – Namiki, Tsukuba, Japan.

[5] Brazilian Nanotechnology National Laboratory (LNNano), Brazilian Center for Research in Energy and Materials (CNPEM), Zip Code 13083-970, Campinas, Sao Paulo, Brazil.

[6] Applied Physics Department, Gleb Wataghin Physics Institute, University of Campinas (Unicamp), Zip Code 13083-859, Campinas, SP, Brazil.

[7]Department of Physics & Astronomy, Texas A&M University, College Station, Texas 77843-4242, United States.

*Corresponding authors: francisco.maia@lnls.br / raul.freitas@lnls.br

1. The Fano model

The Fano effect[1] for graphene systems[2,3] has been attributed to the interaction of the G band vibration and broadband electronic response giving rise to asymmetric resonances in the infrared absorption spectrum. The analytic expression of the Fano resonance E_{Fano} is given by eq. S1 as a function of the excitation frequency ω, phonon frequency ω_0, damping Γ, transition dipole strength of coupled mode p, and dimensionless Fano coupling f. As commonly understood, f corresponds to the transition dipole strength between the discrete and continuum states. In our systems, the Fano effect arises from the interaction of the hyperbolic phonon-polariton (HPhP) modes of the hBN, which are discrete states, with the surface plasmons from graphene that can be described as broadband electronic oscillations in mid-IR range. Thus, f gives information on the coupling strength of the hybrid hyperbolic plasmon phonon-polariton (HP^3) modes.

Here, we extend the Fano resonance (eq. S1), which is given for one oscillator, to the eq. S2 that is sum over *j* discrete HPhP resonances, and a complex non-resonant background E_{nr}[4,5]. In our model, the squared modulus $|E_{HP^3}|^2$ (eq. S3) gives the SINS amplitude. Note that eq. S3, for only one discrete mode and without E_{nr}, becomes equal to the eq. S1.

Particularly, the Fano model assumes that each phonon mode can individually interact with the broadband plasmons, thus each HP^3 mode contains an intrinsic Fano factor. Different Fano factors define particular line-shapes for the resonance, as can be seen in Fig. S1. This implies that the inherent interference between adjacent resonances determine the overall amplitude.

$$E_{Fano}(\omega) \propto \frac{p\big(f\Gamma + (\omega - \omega_0)\big)^2}{(\omega - \omega_0)^2 + \Gamma^2} \qquad \text{eq. S1.}$$

$$E_{HP^3}(\omega) \propto \sum_j \frac{\sqrt{p_j}\big(f_j\Gamma_j + (\omega - \omega_{0j})\big)}{(\omega - \omega_{0j}) + i\Gamma_j} + E_{nr} \qquad \text{eq. S2}$$

$$|E_{HP^3}|^2 = \left| \sum_j \frac{\sqrt{p_j}\big(f_j\Gamma_j + (\omega - \omega_{0j})\big)}{(\omega - \omega_{0j}) + i\Gamma_j} + E_{nr} \right|^2 \qquad \text{eq. S3.}$$

Using the eq. S3, we have fitted, with good agreement, the type I band amplitude spectra of G-hBN on distinct substrates and of G-hBN/Au upon different gate voltages as shown in the main manuscript.

The fitting procedure consisted in keeping the same number of modes and their respective resonance frequencies for all spectra, while no constraints were put on the other parameters. These criteria reasonably assumed that the substrate influence and the bias neither create novel resonant modes nor cause appreciable shift in the resonant frequencies since those properties are mostly associated with the crystalline structure that remains unaltered in our experiments.

Depending on the bottom media for G-hBN, i. e., SiO_2, Au or air in our case (Fig. 1 and 2 of the main manuscript), f can assume different values. In particular for the mode at 815 cm^{-1}, we find f = -30.5 for G-hBN/Au, f = 9.2 for G-hBN/SiO_2 and f = 4.4 for G-hBN/air. As addressed in the main manuscript, the large negative f for G-hBN/Au, compared to those for the other media, is related to an important contribution of Au plasmons in the HP^3 coupling.
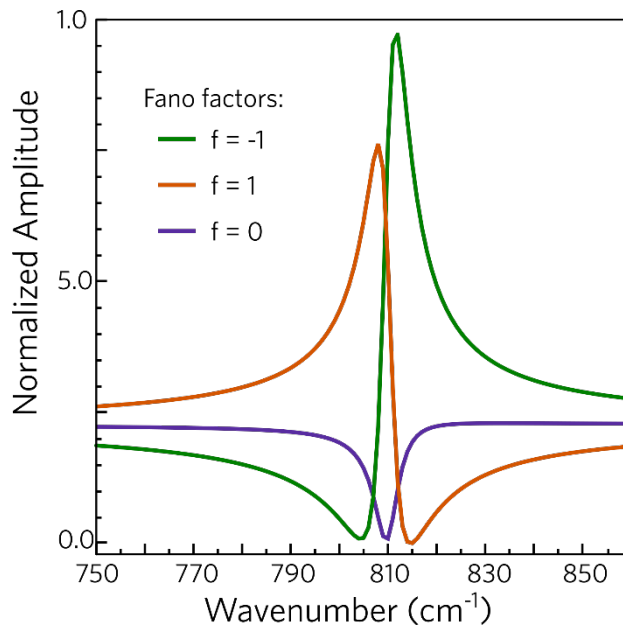
Figure S1| Fano-like spectral intensities (eq. 2) are plotted considering three different values of f with ω_0 = 810 cm^{-1}, p = 1, Γ = 5 cm^{-1} and E_{nr} = $e^{i\pi/4}$. One sees that despite that the parameters associated with the vibrational resonance are kept unaltered, small variations of f leads to very distinguished line-shapes.

2. Frequency-Momentum Dispersion Relation and Surface Reflection Calculation for G-hBN on Air and Gold Substrates

We calculate the frequency-momentum dispersion relation for the type II HP^3s for Au and air substrates (Fig. 4a of the main text) through the reflection coefficient of the surface of the air/G-hBN/substrate layered system. Polariton resonances occur at the divergences of this reflection coefficient[6]. Due to its hyperbolic dispersion, hBN supports multiple discrete polariton dispersion branches

with momenta q_n indexed by integers n = 1,2,... so that q_n increases with increasing n [7–9]. The dispersion relations of the first two branches for each substrate are plotted in Fig. 4a of the main text for the type II band (for type I band see Figure S3a). For the type II band, the Au substrate promotes higher values of in-plane HP³ momenta than the air region for the same mode index n. Conversely, type I modes on the air region have higher in-plane HP³ momenta than on the Au region (Figure S3a). Hence, the structure of polariton modes in G-hBN/air is different from that in G-hBN/Au leading to a mismatch of momenta at the G-hBN(air-Au) junction. Since the dispersion in bulk hBN is hyperbolic, any polariton with a high in-plane momentum has also a high vertical component of momentum. For a waveguide mode, this translates into a high degree of confinement (ratio between free-space wavelength and polariton wavelength in the crystal). It is then straightforward to see that a given transverse mode, from a high-momentum (strong-confinement) region, scatters with high efficiency into a set of transverse modes in a region with a lower confinement, which is the case for the in-plane polarized HP³ modes propagating from Au to air sides. Whereas, the same process originated from the opposite side is much less efficient[10].

To compute the expected polariton reflection properties, we consider in-plane polarized polariton modes travelling from a region with in-plane polariton momenta q_n into a region with different momenta q'_n. Since the tip primarily excites the n = 1 mode, we only consider the transmission of the mode with momentum q_1 across the substrate interface. In this case, the polariton reflection coefficient can be approximately calculated as

$$r = \frac{q'_1 - q_1}{q'_1 + q_1} \prod_{n=2}^{s} \frac{(1 - q_1/q'_n)(1 + q_1/q_n)}{(1 - q_1/q_n)(1 + q_1/q'_n)} \qquad \text{eq. 3}$$

where the product is over mode indices up to integer s [11]. To simplify the calculation, we neglect contributions from mode indices with $n > 2$, since the first two modes with the smallest momenta will dominate the reflection coefficient. The results are shown in Fig. 4b of the main text. The calculated reflection coefficients show pronounced asymmetry, with higher values for polaritons travelling from a low-momentum region to a high-momentum region. This is because polaritons with low q_1 can only efficiently couple to the lowest polariton branch with momentum q'_1. However, for the case where $q'_1 < q_1 < q'_2$, there is significant transmission into both polariton branches. While the excitation of the n = 2 mode has been observed previously[12], its excitation efficiency and, therefore, its role in the propagation regulation is weaker compared to the n = 1 mode. Thus, there is higher coupling efficiency for polaritons travelling from a high momentum region to a low momentum region. This steers to strong reflection of type II modes

when travelling from the air region to the hBN/Au region, and conversely, of type I modes travelling from the Au to the air substrates.

We observe in the Fig. 4a of the main manuscript a small difference between calculated and model-extracted HP^3 momenta for the Au substrate. This can arise from the fact that the calculation of the reflection coefficient of the surface of the air/G-hBN/substrate layered system assumes a perfectly flat Au surface, albeit its roughness is ca. 8 nm RMS. Moreover, this model assumes, for simplicity, the Au as a thin and infinity film in the x-y plane, whilst, G-hBN lies on Au stripes (see Fig. 1 of the main manuscript and Fig. S5), with two well determined edges along x. These sample features can imply boundary conditions not included in the referred calculations and, accordingly, can produce such divergence.

3. Calculated Dispersion Relations and Reflection Coefficient of Type I Band on Au and Air Substrates

Fig. S3a presents the calculated dispersion relation of type I HP^3 modes on air and Au substrate. The calculated reflection coefficient for the type I band (Fig. S3b) indicates the asymmetric reflection coefficient for out-of-plane modes launched on air and Au sides. The understandings on power flow and waves interferences for the HP^3 modes addressed for the type II band, in the main manuscript, hold true for the type I band, however, in this band HP^3 momenta on air are higher than on Au. Hence, in analogy to type II discussion, there is a momenta mismatch for type I HP^{3}s at the air-Au substrate transition leading to reflection of those modes. This is experimentally supported by the oscillations observed in the amplitude narrowband maps and in the amplitude profiles shown, respectively, in Fig. S3c and Fig. S3d.
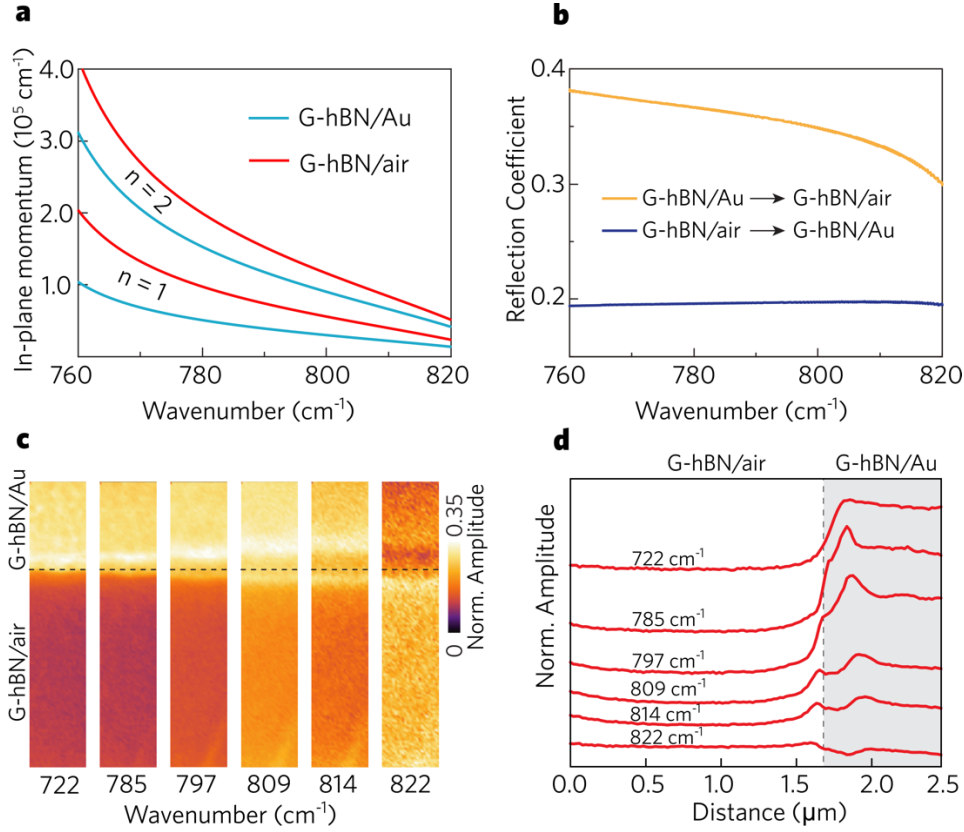
Figure S2| (**a**) Frequency-momentum dispersion relation calculations of the HP^3 modes calculated for type I band regarding the two heterostructures. (**b**) Reflection coefficient calculated from eq. 3 for type I HP^3 modes propagating from G-hBN/air to the G-hBN/Au heterostructure (blue curve) and in the opposite direction (yellow curve). (**c**) Single-frequency amplitude maps of a 35 nm thick G-hBN, on a 0.5 µm x 2.5 µm region with the underneath air-Au junction (air-Au transition is marked by the dashed lines), for different excitation wavenumbers in the type I band. (**d**) Amplitude profiles extracted from the amplitude maps in **d**.

4. Hybridization of Au Surface Plasmons and Type I Band hBN Hyperbolic Phonon-Polaritons

Hybridization of Au surface plasmons (SP) and HPhP of the hBN is shown in the spectral linescan of a hBN crystal lying on Au substrate (Fig. S3a). In the hBN/Au side, the characteristic type I band of hBN/Au is seen, yet, on the Au side a spatio-spectral resonance (arrow in the Fig. S3a) rises extending from the locations 3.2 µm (crystal edge) to 7.2 µm and with maximum centered near 814 cm^{-1}. Comparing the spectral linescans of hBN/Si (Fig. S3b) and hBN/SiO$_2$ (Fig. S3c), we note that such resonant feature does not appear neither in Si nor SiO$_2$ surfaces. Since the Au substrate is spectrally non-resonant, we attribute such resonance to the SP-HPhP hybridized modes. In this case, on the Au side the tip launches IR broadband SPs that propagate up to the crystal edge wherein form hybrid SP-HPhP modes. By transmission, SP-HPhP modes travel inside hBN/Au. Reflected SP-HPhP modes form the spatio-spectral resonance on the Au side of the Fig. S3a. These results allow stating the participation of the SP-HPhP hybridization in the HP^3 coupling observed in the G-hBN/Au heterostructure.
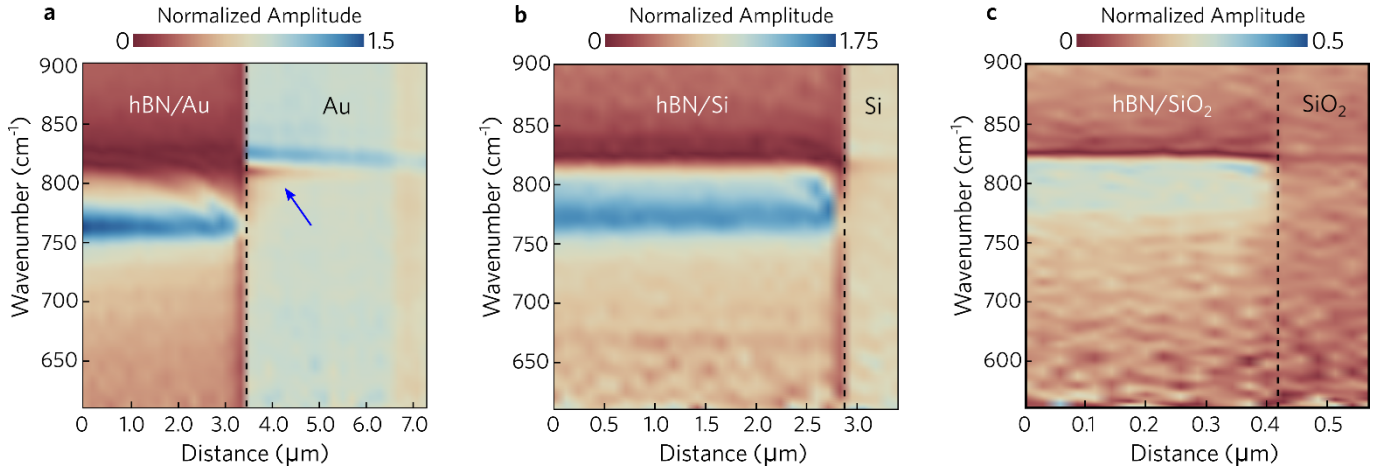
Figure S3| Spectral linescans of the type I of hBN crystal lying on Au (**a**), Si (**b**) and SiO₂ (**c**) substrates. The vertical dashed lines mark the edge of the crystals. The blue arrow in (**a**) indicates a spatio-spectral resonance, spanning from the crystal edge to 7.2 μm with maximum near 814 cm⁻¹.

5. Modelling the HP³ waves in the G-hBN Heterostructure Bridging the Au-air Junction

The G-hBN/Au and G-hBN/air junction can be seen as a general case of a two-dimension crystal lying onto junction of the media 2 and 3 (Figure S4). These media alter the dielectric environment creating media 1 and 2 in the crystal.

In the s-SNOM experiment, free-space far-field radiation is confined into sub-diffractional volumes via antenna effect at the metallic tip[13]. For mid-IR radiation, the illumination spot includes not only the tip but also a portion of the sample's surface (Figure S5a). Therefore, any metallic object with dimensions $\sim \lambda/2$ can work as an antenna, such as the AFM tip, metallic rods and graphene flakes edges. Sharp regions of those objects (e.g. tip apex and metallic sample's edges) can hold high density of confined fields (large momentum) and, hence, are potential launchers of polaritonic waves when in contact with a polaritonic media, as in the case of this work wherein Au edges represent such sharp metallic objects launching HP³s in G-hBN (Figure S5). In our model, the resulting optical near-field ξ_{opt} is determined by the near-field interaction produced by the most efficient launchers: i) AFM tip apex (optical near-field ξ_{Tip}) and ii) Au edges (optical near-field ξ_{Au}).

In our case represented in the Figure S5a, media 1, 2, 3 and 4 are, respectively, G-hBN/air, G-hBN/Au, air and Au. We consider the reference frame in the Figure S5b (same as Fig. 4c of the main manuscript). Tip at x launches circular waves A_{out} and A'_{out} that propagate to and reflect at the junctions at x = 0 and x= x_edge. The reflected waves A_{ref} and A'_{ref} travel back to the tip. These waves are the first and second terms in the expression of ξ_{Tip} (eq. S3, the same as eq. 4 of the main manuscript) with amplitude

7

A and the arbitrary phases α_1 and α_2. Note that such circular waves decay as $1/\sqrt{d}$, where d is the propagated distance from the source. In the case of the tip-launched waves, the tip is the source, hene, d is twice the tip-edge distance (standing waves). As mentioned in the main manuscript, the term $Ce^{-i\eta}$ (eq. S3) takes in account contributions from (i) a local dielectric near-field interaction between tip and sample, which is independent on tip position, and (ii) a non-resonant background originating from other scattering centers coexisting in the far-field illuminated confocal spot.
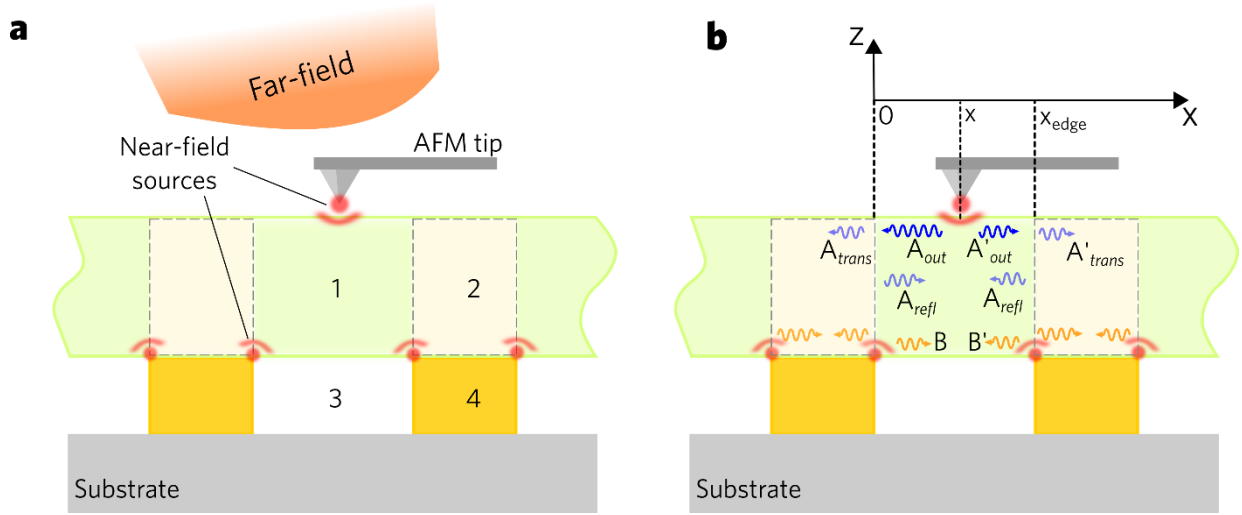
Figure S4| (**a**) Scheme of the main antennas responsible for the near-field sources is our system. (**b**) reference frame and representation of the waves taken into account for the ξ_{Opt} modelling. Tip launched circular waves are represented by the outgoing A_{out} and A'_{out}. Those waves propagate to the G-hBN/(air-Au) junction, wherein, they reflect and propagate to the tip as the A_{refl} and A'_{refl} waves. A_{trans} and A'_{trans} are the transmitted waves across the junctions. B and B′ represent Au edges-launched waves.

The optical field ξ_{Au} (eq. S4, the same as eq. 5 of the main paper) is formed by waves B and B′, respectively, launched by the edges at x = 0 and at x= x_{edge}. B_0 and B_1 are the amplitude and β_0 and β_1, the arbitrary phases, of these waves. We assume the Au edge-launched waves to decay as $1/d$ since we treat the edges as a linear series of point sources launching spherical waves inside the hBN crystal. The same decay rate was successfully applied by A. Woessner *et al.*, Nature Materials [14] for modeling the plasmons launched by a graphene edge in a similar G-hBN heterostructure. All waves possess the same complex momentum $Q = q_1 + i\kappa_1$. Hence, tip and Au edges produce $\xi_{Opt} = \xi_{Tip} + \xi_{Au\ edges}$, which is the near-field scattered by the tip at x. The amplitude of ξ_{Opt} is used to fit the amplitude oscillations of the Fig. 4e of the main paper. Note that this picture remains valid for the tip on the G-hBN/Au and G-hBN/Au regions.

$$\xi_{Tip} = A\left(\frac{e^{-i\alpha_0}\, e^{i(q_1 + i\kappa_1)2x}}{\sqrt{2x}} + \frac{e^{-i\alpha_1}\, e^{i(-q_1 + i\kappa_1)2(x_{edge}-x)}}{\sqrt{2(x_{edge}-x)}} \right) + Ce^{-i\eta} \qquad \text{eq. S4}$$

8

$$\xi_{Au\ edges} = B_0 \frac{e^{-i\beta_0}\, e^{i(q_1 + i\kappa_1)x}}{x} + B_1 \frac{e^{-i\beta_1}\, e^{i(-q_1 + i\kappa_1)\left(x_{edge}-x\right)}}{\left(x_{edge}-x\right)} \qquad \text{eq. S5}$$

The model-extracted amplitudes and complex momenta allow us to obtain the launcher efficiency (σ) for the tip $\sigma_{Tip} = 8\pi[A]^2$ and the Au edges $\sigma_{Edge} = (B_0 + B_1)^2$ [15] presented in Table S1 for air and Au substrates. Likewise, we are able to provide the damping of each type II HP^3 wave for the two substrates in the Table S2.

Table S1| Launcher efficiency for tip (σ_{tip}) and Au edge (σ_{Au}) on different materials.

	air		Au	
ω (cm^{-1})	σ_{Tip} (cm^{-2})	σ_{Au} (cm^{-1})	σ_{Tip} (cm^{-2})	σ_{Au} (cm^{-1})
1425	81	1.8	0.16	0.05
1433	73	1.2	0.5	0.04
1450	56	0.5	1.0	0.03
1466	36	0.7	2.3	0.25

Table S2| Damping of the type II HP^3 modes for Au and air substrates.

	Damping (k/q)	
ω (cm^{-1})	air	Au
1425	0.13	0.02
1433	0.15	0.1
1450	0.17	0.2
1466	0.18	0.23

6. References

[1]   U. Fano, *Phys. Rev.* **1961**, *124*, 1866.

[2]   T.-T. Tang, Y. Zhang, C.-H. Park, B. Geng, C. Girit, Z. Hao, M. C. Martin, A. Zettl, M. F. Crommie, S. G. Louie, Y. R. Shen, F. Wang, *Nat. Nanotechnol.* **2010**, *5*, 32.

[3]   Z. Li, C. H. Lui, E. Cappelluti, L. Benfatto, K. F. Mak, G. L. Carr, J. Shan, T. F. Heinz, *Phys. Rev. Lett.* **2012**, *108*, 1.

[4]   B. Pollard, F. C. B. Maia, M. B. Raschke, R. O. Freitas, *Nano Lett.* **2016**, *16*, 55.

[5]   F. C. B. Maia, P. B. Miranda, *J. Phys. Chem. C* **2015**, *119*, 7386.

[6]   S. Dai, Z. Fei, Q. Ma, A. S. Rodin, M. Wagner, A. S. McLeod, M. K. Liu, W. Gannett, W. Regan, K. Watanabe, T. Taniguchi, M. Thiemens, G. Dominguez, A. H. C. Neto, A. Zettl, F. Keilmann, P. Jarillo-

Herrero, M. M. Fogler, D. N. Basov, *Science (80-.).* **2014**, *343*, 1125.

[7] Y. He, S. He, J. Gao, X. Yang, *J. Opt. Soc. Am. B* **2012**, *29*, 2559.

[8] A. Poddubny, I. Iorsh, P. Belov, Y. Kivshar, *Nat. Photonics* **2013**, *7*, 948.

[9] S. Dai, Q. Ma, M. K. Liu, T. Andersen, Z. Fei, M. D. Goldflam, M. Wagner, K. Watanabe, T. Taniguchi, M. Thiemens, F. Keilmann, G. C. a. M. Janssen, S.-E. Zhu, P. Jarillo-Herrero, M. M. Fogler, D. N. Basov, *Nat. Nanotechnol.* **2015**, *10*, 682.

[10] D. Jalas, A. Petrov, M. Eich, W. Freude, S. Fan, Z. Yu, R. Baets, M. Popović, A. Melloni, J. D. Joannopoulos, M. Vanwolleghem, C. R. Doerr, H. Renner, *Nat. Photonics* **2013**, *7*, 579.

[11] C. Dragone, *IEEE Trans. Microw. Theory Tech.* **1984**, *MTT-32*, 1319.

[12] S. Dai, Q. Ma, T. Andersen, a. S. Mcleod, Z. Fei, M. K. Liu, M. Wagner, K. Watanabe, T. Taniguchi, M. Thiemens, F. Keilmann, P. Jarillo-Herrero, M. M. Fogler, D. N. Basov, *Nat. Commun.* **2015**, *6*, 6963.

[13] F. Keilmann, R. Hillenbrand, *Philos. Trans. R. Soc. A Math. Phys. Eng. Sci.* **2004**, *362*, 787.

[14] A. Woessner, M. B. Lundeberg, Y. Gao, A. Principi, P. Alonso-González, M. Carrega, K. Watanabe, T. Taniguchi, G. Vignale, M. Polini, J. Hone, R. Hillenbrand, F. H. L. Koppens, *Nat. Mater.* **2014**, *14*, 421.

[15] S. Dai, Q. Ma, Y. Yang, J. Rosenfeld, M. D. Goldflam, A. McLeod, Z. Sun, T. I. Andersen, Z. Fei, M. Liu, Y. Shao, K. Watanabe, T. Taniguchi, M. Thiemens, F. Keilmann, P. Jarillo-Herrero, M. M. Fogler, D. N. Basov, *Nano Lett.* **2017**, *17*, 5285.